

# Automatic Detection of Coronal Holes and Study their Properties

Dr Gavisiddappa <sup>1</sup>, Venuchandan M G<sup>2</sup>

<sup>1</sup>Artificial Intelligence & Data Science, CIT, Gubbi

<sup>2</sup>Artificial Intelligence & Data Science, CIT, Gubbi

\*\*\*

**Abstract** – Coronal hole is the outer most part of the sun's atmosphere where it is a region with low plasma density and open magnetic field lines in solar corona to understand its solar wind generation and space weather phenomena, this makes them to look dark region on the sun. And the causes done by sun's radiation solar wind effect on Earth's atmosphere and also on ground and it mainly causes some communication and appearing of aurora on North-pole and South-pole. By using pretrained machine learning model it uses neural network to detect the coronal and by using traditional method intensity-thresholding technique to detect the coronal hole using images taken from Solar Dynamics Observatory's Atmospheric Imaging Assembly (SDO/AIA). It includes high resolution images for segmentation and parameter extraction using morphological evolution of coronal holes driven by solar magnetic. Extracting the parameters like centroid, area, latitude-longitude and intensity where analyzed after contouring the coronal hole revealing correlation with solar cycle variations in geomagnetic disturbances. Comparing the coronal hole with sunspots, it is eleven years process for analyzing the coronal hole and its properties. It helps to study about evolution of coronal hole and coronal mass ejection.

**Key Words:** numpy, skimage, morphology, CNN, CHRONNOS, data analysis

## 1.INTRODUCTION

The solar corona, the Sun's outermost atmosphere, is a captivating spectacle typically visible only during a total solar eclipse. This ethereal halo, composed of superheated plasma, reaches temperatures of millions of degrees Celsius, despite its extremely low density. Though faint, the corona's intricate structure, marked by coronal loops, solar filaments, coronal holes, streamers, and bright points, offers valuable clues about the Sun's magnetic activity and its influence on space weather. While its feeble light makes it challenging to observe directly, specialized telescopes like coronagraphs and instruments sensitive to UV and X-ray radiation enable scientists to study this dynamic region, providing crucial insights into our star's

behavior. The Sun's activity, including sunspot formation and coronal brightness, follows an approximately 11-year cycle. During solar maxima, the corona becomes more active, exhibiting increased brightness in UV, EUV, and X-ray wavelengths, as well as a higher number of bright points, active region loops, and coronal holes. Conversely, during solar minima, the corona is less active, with reduced brightness and fewer features. Understanding these cyclical variations in the solar corona is a crucial for predicting and mitigating the effects of space weather, which can impact Earth's environment and technological systems. Coronal holes, dark regions visible in EUV and X-ray wavelengths, are low-density areas in the Sun's corona where open magnetic field lines allow high-speed solar wind to escape into space. These holes can appear on the Sun's disk at various latitudes, including the polar regions. The lower temperature within coronal holes, compared to the surrounding corona, contributes to their distinct appearance. As open magnetic field lines rise from the Sun's surface and expand into the corona, they form the characteristic structure of coronal holes, which play a significant role in shaping the solar wind and influencing space weather conditions.

The concept of coronal holes was first introduced by E.W. Maunder in 1905 [1], who indirectly linked recurrent geomagnetic disturbances to solar activity. Julius Bartels further refined this idea in the 1930s, identifying these disturbances as "M-region" [1]. Direct observations of coronal holes, including their lower emission, temperature, and density compared to the quiet Sun, became possible with the advent of X-ray and EUV telescopes in the 1960s and 1970s. The launch of Skylab in 1973 significantly advanced our understanding of coronal holes, revealing their stability during the Sun's rotation and their distinct appearance in various wavelengths. Subsequent missions, such as SOHO, with improved spatial resolution, have further enhanced our ability to study these enigmatic features and their impact on space weather [1]. The solar wind, originating from coronal holes, significantly impacts space weather. Fast and

dense solar wind can trigger severe geomagnetic storms, affecting astronauts, navigation systems, and communication networks. To better understand the mechanisms behind solar wind generation and its variability over the solar cycle, we analyze data from the Atmospheric Imaging Assembly instrument on board the Solar Dynamics Observatory. Specifically, we utilize 17.1 nm images to detect and track coronal holes using image processing techniques. This study delves into the characteristics of coronal holes, their evolution, and their association with solar wind properties. The findings contribute to our understanding of space weather and help in forecasting potential disturbances.

## 2. LITERATURE REVIEW

### A. Corona:

The corona, a solar atmosphere layer, is visible only during total solar eclipses or through specialized instruments called coronagraphs that obscure the sun's bright disk. Its shape fluctuates based on the sun's global magnetic configuration, known as the solar cycle. During solar maximum, the corona is observable along the entire limb due to shrinking polar coronal holes and widespread active regions. At solar minimum, bright coronal structures like streamers appear closer to the equator, while active regions concentrate near the solar equator because of extensive open polar magnetic fields. Space-based sensors can detect the corona on the solar disk using X-ray or EUV wavelengths, revealing high-temperature phenomena such as loops and filament eruptions (flares, coronal mass ejections) with temperatures in the millions of degrees. Coronal holes, being less luminous and less dense than other quiet solar areas, are also detectable at these wavelengths. The corona's density is at least  $10^{10}$  times lower than the photosphere's, yet its temperature is significantly higher, exceeding one million degrees [1].

### B. The Coronal Hole:

Coronal holes exhibit reduced emission at X-ray and Extreme Ultraviolet (EUV) wavelengths due to their lower coronal temperature and density, appearing darker than surrounding regions [3][4][5][6]. Figure 2.1 displays a high-resolution image of a coronal hole captured by the Solar Dynamic Observatory Atmospheric Imaging Assembly (SDO/AIA). These low-density areas in the solar corona feature open magnetic field lines, allowing high-speed solar wind to escape into space. Their occurrence and characteristics vary significantly

throughout the 11-year solar cycle due to the sun's changing magnetic field. Coronal hole plasma and quiet sun (QS) regions differ not only in their features but also in their fundamental magnetic configurations. QS areas are dominated by small and large closed magnetic fields, known as magnetic carpets, while coronal holes are characterized by consolidated unipolar open magnetic fields. These open field lines are brought to the solar surface by convection beneath the photosphere, causing them to cluster. Examination of the photospheric origins of coronal hole open field lines reveals their concentration in intergranular lanes.

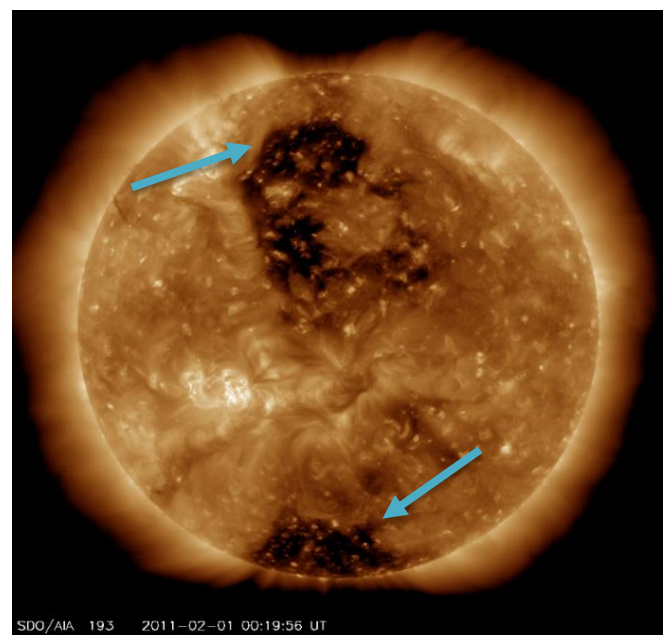


**Fig-2.1** Coronal hole taken by SDO/AIA

While coronal holes (CHs) and quiet Sun (QS) regions have distinct magnetic configurations, they also exhibit different properties. CHs consist of concentrated unipolar open magnetic fields, whereas QS areas feature both small and large closed magnetic fields. The open field lines in CHs are brought to the solar surface by convection beneath the photosphere, causing them to cluster. As altitude increases above the photosphere, the decreasing density and pressure allow the open magnetic flux tubes to expand, forming what is observed as a CH at coronal altitudes [7][8]. Various wavelengths are used for analysis, corresponding to different temperatures. Higher temperature objects emit radiation at shorter wavelengths, while lower temperature objects emit radiation at longer wavelengths.

### C. Observation of Coronal Hole:

Coronal holes were first indirectly identified by E.W. Maunder in 1905, who linked recurring 27-day geomagnetic disturbances to solar activity. In the 1930s, Julius Bartels further analyzed these disturbances using

statistical methods, dubbing them "M-regions." Direct observations of coronal holes became possible in the 1960s and 1970s with the introduction of X-ray and EUV imaging technology, which revealed their reduced emission, temperature, and density compared to the quiet Sun (QS). The launch of Skylab in 1973 marked a significant advancement in coronal hole studies, demonstrating their resistance to the Sun's asymmetric rotation. Coronal holes were also detected in He I 10830 Å images, appearing brighter than the QS due to their lower density and emission. Observational technology has since progressed from Skylab to SOHO (1995) with 2.6 arcseconds per pixel resolution, Hinode (2006) with 1 arcsecond per pixel, and the Solar Dynamics Observatory (SDO) offering 1 arcsecond per pixel and a temporal resolution of 10 seconds, greatly enhancing coronal hole research. These contemporary instruments, capable of detecting dominant magnetic polarity, have improved the visual identification of coronal holes. Long-term studies spanning entire solar cycles have been facilitated by data from instruments such as SOHO/EIT and MDI, operational since 1995. This has provided an extensive dataset for examining coronal hole behavior over prolonged periods [1].

#### D. Space Weather:

Modern society's growing dependence on sophisticated technologies has made it more susceptible to space weather effects. Despite substantial advancements in comprehending the physical mechanisms connecting solar activity to geomagnetic storms over the last five decades, accurately forecasting the timing, length, and intensity of Earth-bound space weather phenomena remains a significant obstacle. Predicting eruptions from solar regions prone to flares or coronal mass ejections (CMEs) poses considerable difficulties. Although numerous models have been created, their ability to predict flares and CMEs accurately remains limited [17].

A crucial aspect of space weather prediction involves determining whether a flare or CME is directed towards Earth and evaluating its potential geoeffectiveness. Forecasts for geomagnetic storms must include estimates of the storm's duration, expected end time, and projected arrival time at Earth. The Space Weather Prediction Center (SWPC) has developed three scales to categorize space weather events based on their origin, with each scale ranging from 1 (minor) to 5 (extreme) [9].

The Radio Blackout Scale assesses the impact of X-ray radiation on the ionosphere using data from geostationary satellites. Sudden ionospheric disturbances (SIDs), resulting from increased X-ray radiation, enhance ionization in the daytime ionosphere, disrupting telecommunications and other communications. These disturbances affect high-frequency radio bands, causing scintillation, phase shifts, and altered signal propagation

paths. However, television and commercial radio broadcasts, which rely on ground-based towers, typically remain unaffected.

The Geomagnetic Storm Scale evaluates the impact of powerful solar events, particularly CMEs. The plasma expelled during CMEs contains magnetic clouds that can induce strong magnetic currents in the magnetosphere, ionosphere, and Earth's surface. If these magnetic clouds have a strong southward orientation, they can reconnect with Earth's predominantly northward magnetic field, intensifying geomagnetic disturbances. The 1989 Quebec blackout exemplified how these currents can disrupt power grids and damage transformers through overheating and mechanical vibrations.

Magnetospheric reconnection occurs when southward interplanetary magnetic fields (IMFs) interact with Earth's dayside magnetic field, extending into the magnetotail, as described in Dungey's 1963 model. A secondary reconnection at high latitudes directs solar particles toward the poles, resulting in auroras and geomagnetic disturbances. While auroras, as shown in Fig. 2.3, are visually striking, they are accompanied by environmental disruptions.



Fig-2.3 Aurora seen in Northern Norway

#### E. Evolution of short-term coronal hole

Evolution occurs over days to week driven by sun's magnetic field. It is thought that magnetic reconnection between the open magnetic fields of CHs and tiny closed magnetic fields observed in the (QS) and within CHs itself generates small-scale morphological alterations. In order to quantify the magnetic reconnection rate and the diffusion coefficient that are causing these contacts, this process is examined using methods such as CHEVOL. It is a method related to coronal mass ejection, It entails examining CH boundary changes in displacement. On shorter timeframe this small-scale dynamic boundary causes flux in the development of coronal holes, magnetic reconnection between the open magnetic fields of CHs and tiny closed in QS and within the CHs itself causes small-scale morphological alterations. Small-scale boundary changes have only recently been thoroughly investigated with high-resolution measurements, but large-scale and long-term CH development, including changes in area, magnetic flux, and their function in the

Sun's dipole reversal, has been thoroughly researched across solar cycles. Early studies in the 1970s demonstrated that magnetic reconnection and bright spots, which might promote the spread of open flux, have a strong connection to those transient changes [14].

### 3. METHODOLOGY

#### 3.1 Multi-Channel Coronal Hole Detection

This research utilized a convolutional neural network (CNN) to identify and outline coronal hole boundaries using data from seven extreme ultraviolet (EUV) channels of the Atmospheric Imaging Assembly (AIA) and line-of-sight magnetograms from the Helioseismic and Magnetic Imager (HMI) on the Solar Dynamics Observatory (SDO). The main model, CHRONNOS (Coronal Hole Recognition Neural Network Over Multi-Spectral Data), employs a network approach that grows progressively to boost training efficiency, create detailed segmentation maps, and capture relationships across the solar disk. CNNs are particularly adept at processing high-dimensional data, such as images[10], due to their structure, which consists of layers of convolutional operations. Each layer contains filters (kernels) with learnable weights that perform convolutions on feature maps from previous layers, converting the input into increasingly abstract representations. Through supervised training with backpropagation using a dataset of input-output pairs, the network's weights are adjusted, allowing the model to effectively generalize to new, unseen data[11].



**Fig-3.1** Composite multi-channel observation from SDO AIA to detect coronal hole by CHRONNOS model.

#### 3.1.1 Dataset Collection

The dataset incorporates seven EUV filters from the AIA (94 Å, 131 Å, 171 Å, 193 Å, 211 Å, 304 Å, 335 Å) and magnetograms from the HMI on SDO. Supervised training utilized pixel-wise segmentation masks as ground truth. The network successfully generalized its coronal hole detection abilities despite minor data variations. To ensure dataset consistency, preprocessing addressed device degradation and annual fluctuations caused by the spacecraft's ecliptic orbit [12]. Images were

scaled to 512×512 pixels, yielding a spatial resolution of 4.2" per pixel, which was adequate for detecting even small coronal holes. The CATCH algorithm, a threshold-based technique, was employed to identify coronal holes in AIA 193 Å filtergrams. The algorithm determined boundaries reflecting temperature and density gradients by minimizing area differences across thresholds. Only well-defined coronal holes with distinct boundaries were chosen.

#### 3.1.2 Progressive Growing Neural Network (CHRONNOS)

ConvBlocks serve as the primary trainable elements in the CHRONNOS model. These blocks form the basis of the network architecture, which uses a progressive growth approach during training. This method introduces a new branch consisting of convolutional layers and stride-2 convolutions, reducing spatial resolution by half. An average pooling layer adjusts the input image's spatial dimensions to match the previous convolutional layer's output. Progressive growing allows the model to generate high-resolution segmentation maps while exploiting multi-wavelength data to detect inter-channel relationships. The encoder-decoder architecture incorporates skip connections, which maintain spatial details and enhance gradient updates [13], facilitating the detection of smaller coronal regions and improving segmentation accuracy[14].

For computational feasibility, the model operated on 512×512 pixel images, capturing necessary spatial details. The model used pre-trained weights and was connected to the Joint Science Operations Center (JSOC) via the drms package to download and verify data. However, issues with missing headers in contour-detected maps and challenges with the JSOC data center led to the exclusion of this method. Figure 3.2 illustrates the contour-detected maps, but limitations with header information prevented parameter extraction from the detected regions[2].

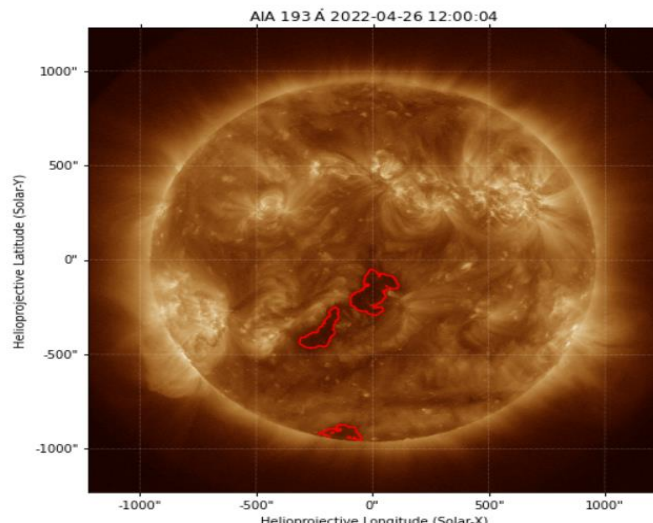


**Fig-3.2** Detection of coronal hole using pretrained CHRONNOS model.

### 3.2 DETECTION USING INTENSITY AND THRESHOLD.

#### 3.2.1 Finding the Threshold value

This technique employs fundamental commands to identify coronal holes using exclusively AIA 193 Å images (4096x4096 pixels), which are optimal for detecting CHs. These images are in 16-bit fits format (0 to 65535) and are obtained from sources like JSOC, VSO, and SDO, with a daily cadence of 1-lev images. The process involves reading the file and masking the solar limb using the sun radius provided in the header. The x and y axes are converted from arcsec to pixels to calculate the distance from the center to the solar limb. Pythagoras' theorem-(1) is utilized to compute each pixel's distance from the center, masking pixels within the solar limb and marking values outside as nan. A histogram is plotted using a gaussian non-linear quadratic curve-(2), and the full width half maximum (FWHM)-(3) is employed to measure the gaussian curve at half its maximum value, between the rising and falling edges of the histogram. The threshold value is determined using formula-(4), which is then applied to contour the darker regions.

(1)

$$d = \sqrt{(x_2 - x_1)^2 + (y_2 - y_1)^2}$$

(2)

$$y(x) = y_0 + A \cdot e^{-\frac{(x - \mu)^2}{2\sigma^2}} + B \cdot (x - \mu) + C \cdot (x - \mu)^2$$

(3)

$$2w = \sqrt{\frac{2}{\ln 2}} FWHM$$

(4)  $\mu - \sigma$

$\mu - 1.5\sigma$

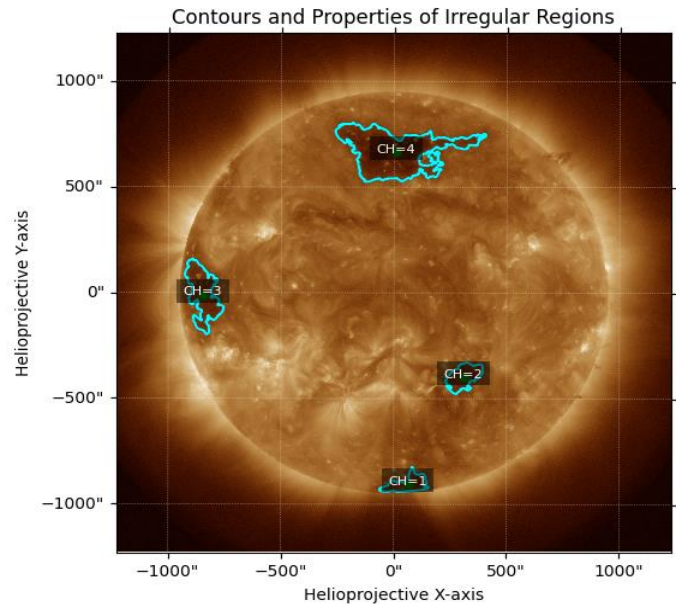
$\mu - 2\sigma$

#### 3.2.2 Delineating the Darker Areas

To detect and outline darker areas, a suitable intensity threshold is employed, utilizing intensity thresholding to differentiate image sections with varying brightness levels. The intensity histogram, exhibiting a multimodal distribution, aids in determining thresholds where frequencies align with image characteristics. To minimize noise and smooth the image, Gaussian filtering is utilized, with an appropriate sigma value chosen for optimal results. Morphological filtering is subsequently applied to link segmented coronal regions, while dilation amplifies pixels within the outlined area. Area thresholding is used to remove smaller, insignificant

outlines. After delineation, the coronal hole (CH) regions are transformed into binary format, with the outlined area set to one and the remainder to zero. The binary image is then multiplied by the original image to derive parameters specific to the delineated region.

Fig-3.3 Detected and labelled CH regions



#### 3.2.3 Parameter Extraction

From the outlined region, it is necessary to compute the area and its centroid corresponding to helioprojective scales. The area calculation employs the shoelace formula (1) for a polygon. The areas depicted in Fig-3.3 are labeled for extracting parameters within the outlined region. After parameter extraction, the data is recorded in a spreadsheet. A linear curve graph is then plotted for the entire eleven-year period and compared with sunspot data, allowing for curve overlay.

$$A = \frac{1}{2} (x_0y_1 - x_1y_0 + \dots + x_{n-2}y_{n-1} - x_{n-1}y_{n-2} + x_{n-1}y_0 - x_0y_{n-1}) \quad \text{-----(1)}$$

### 4. ANALYSIS AND RESULTS

In our model configurations, we employ the Adam optimizer with a 0.001 learning rate,  $\beta_1 = 0$  and  $\beta_2 = 0.99$  [13]. To mitigate overfitting, we implement a weight decay of  $10^{-8}$ , set the dropout layer in each ConvBlock to 0.2, and enhance the images through random horizontal and vertical flips. We utilize binary-cross-entropy as the loss function and apply a weight of 0.1 to the noncoronal-hole class to address class imbalance. We begin with a batch size of 64, reducing it by half at each resolution level, resulting in a batch size of 1 at the highest resolution due to computational constraints. We adjust the number of training epochs similarly, with 10 epochs at the highest resolution and a maximum of 100 epochs. "Recall" denotes the percentage of coronal holes in the manual CATCH labels identified by the evaluated method, "precision" represents the percentage of coronal

holes detected by the evaluated method that are also present in the CATCH labels, and "accuracy" indicates the percentage of correct coronal hole detections.

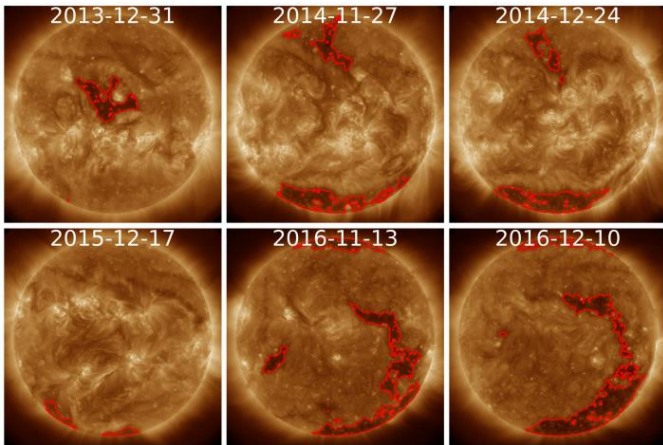
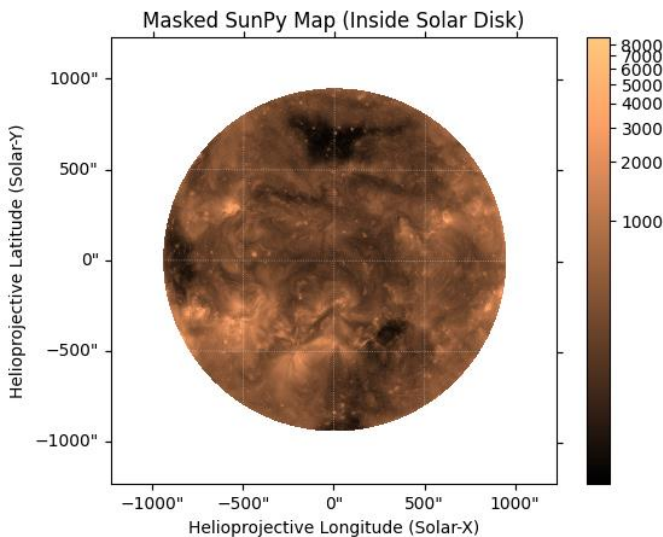


**Fig-4.1** Detection of CH using chronnos pretrained model [2].

To extract pixels within the solar limb, we mask the map using the where command. This allows us to contour only the darker pixels inside the solar limb. To mask these pixels, we convert the sun's radius from arcseconds to pixel coordinates. We determine the thresholding value by plotting a histogram, masking pixels inside the solar limb to obtain intensities greater than zero. Outside the solar limb, a higher number of pixels are closer to zero. This process enables us to measure the distance from the



radius to the limb without altering any header information.

**Fig-4.2** Masked map of pixels inside the solar limb

Following the map masking process, a histogram is created to examine pixel intensity and quantity within the solar limb. The mean is determined by fitting a Gaussian curve to the histogram, with the amplitude indicating the mean value. The sigma value is calculated using the Full Width at Half Maximum (FWHM) of the distribution

curve, as shown in Fig-4.3. The FWHM is defined by the curve's rising and falling edges. To establish an optimal contouring threshold, the difference between mean and sigma is computed. Typical threshold values fall between 100 and 180, with lower values suggesting a reduced likelihood of coronal hole presence.

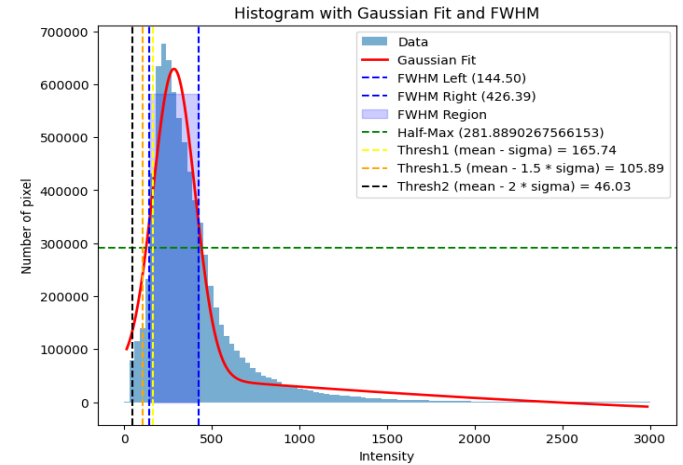


**Fig 4.3** Intensity v/s number of pixels histogram plot

Parameters are extracted from the identified coronal holes (CHs) depicted in Fig-3.3. This extraction involves transforming the image into a coordinate system ranging from  $-90^\circ$  to  $+90^\circ$  in both latitude and longitude. CH coordinates are determined by locating the centroid of each contour region. The polygon shoelace formula is employed to calculate parameters for each contoured area. These values are then recorded in a spreadsheet for subsequent analysis.

Contour Properties with Centroids in Arcseconds and HGS Latitude/Longitude in Degrees:			
Region ID	Centroid (arcsec)	\	
0	(73.0770205432588, -904.1160317619128)		
1	(336.00588832244216, -397.2791036894544)		
2	(-831.55041330331, -2.473817302508648)		
3	(21.7498878071363, 668.3740828501218)		
Contour Area (pixels <sup>2</sup> )	Latitude (HGS, degrees)	Longitude (HGS, degrees)	
0	28347.5	-70.868845	13.631329
1	36788.5	-22.714395	22.592558
2	86719.5	0.922044	-61.546091
3	243692.5	47.136168	1.921055

**Fig-4.4** Extracted parameters of the coronal hole to the image reference to Fig-3.3.

The study of coronal hole evolution spans an 11-year period and is contrasted with sunspot data as a reference point. This comparative analysis involves extracting and recording parameters in a spreadsheet, followed by the creation of graphs illustrating the temporal progression of coronal holes alongside sunspot activity

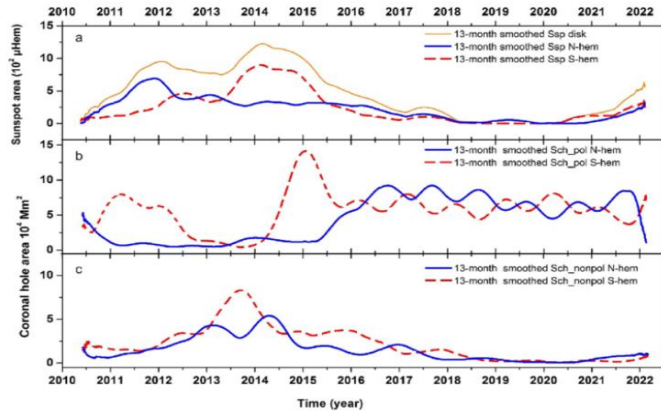


**Fig-4.5** Comparison between sunspot and coronal hole [16].

## CONCLUSION

Coronal holes, located in the Sun's outermost layer, play a critical role in understanding the Sun's magnetic field and solar wind dynamics. Accurate detection of coronal holes is essential for improving space weather forecasting models, which help mitigate the potential impacts of solar events, such as coronal mass ejections, on Earth's technological infrastructure.

The CHRONNOS detector leverages neural networks to analyze coronal holes using multi-channel observations across seven EUV wavelengths, providing detailed segmentation and detection. An alternative method involves intensity-threshold-based techniques, which segment and detect coronal holes by analyzing intensity gradients. By studying the spatial and morphological evolution of these regions over time, researchers can explore the relationship between coronal holes, solar activity, and the quiet Sun.

Traditional image processing methods have enabled precise boundary detection, segmentation, and parameter extraction for coronal holes, often utilizing morphological filtering to enhance accuracy. The CHRONNOS methodology further advances detection precision by integrating data from multiple wavelengths. Extracted metrics, including area, centroid position, and intensity distributions, serve as critical inputs for understanding the role of coronal holes in generating high-speed solar wind streams and forecasting geomagnetic storms.

## REFERENCES

[1]. Larisza D. Krista Boulder, evolution of coronal hole, Colorado, 15 October 2012, arXiv:1210.4475v1  
 [2]. [R. Jarolim](#), [A.M. Veronig](#), [S. Hofmeister](#), [S.G. Heinemann](#), [M. Temmer](#), [T. Podladchikova](#), [K. Dissauer](#), 29 April 2021, Multi-channel coronal hole detection with convolutional neural networks, arXiv:2104.14313v2

[3]. Altschuler, M.D., Trotter, D.E. & Orrall, F.Q. (1972). Coronal Holes. *Solar Physics*, 26, 354–365. 31  
 [4]. Chapman, S.A. & Bromage, B.J.I. (2002). Variation of coronal hole area from solar minimum to maximum using EUV spectroscopic data from SOHOCDs (preliminary results). In A. Wilson, ed., *From Solar Min to Max: Half a Solar Cycle with SOHO*, vol. 508 of ESA Special Publication, 383–385. 31, 86, 91, 92, 118  
 [5]. Del Zanna, G. & Bromage, B.J.I. (1997). Spectroscopic Diagnostics Applied to the August 1996 Equatorial Coronal Hole. In A. Wilson, ed., *Fifth SOHO Workshop: The Corona and Solar Wind Near Minimum Activity*, vol. 404 of ESA Special Publication, 323–+. 31  
 [6]. Vaiana, G.S., Zombeck, M., Krieger, A.S. & Timothy, A.F. (1976). ATM observations - X-ray results. *Astrophysics & Space Science*  
 [7]. Cranmer, S.R. (2009). Coronal Holes. *Living Reviews in Solar Physics*, 6, 3–+. xiii, xiv, 32, 41, 42, 43, 44, 65  
 [8]. Tu, C., Zhou, C., Marsch, E., Xia, L., Zhao, L., Wang, J. & Wilhelm, K. (2005). Solar Wind Origin in Coronal Funnels. *Science*, 308, 519–523. xiii, 31, 33  
 [9]. Biesecker, D.A., Webb, D.F. & St. Cyr, O.C. (2008). STEREO Space Weather and the Space Weather Beacon. *Space Science Reviews*, 136, 45–65. 51  
 [10]. LeCun, Y., Bengio, Y., & Hinton, G. 2015, *nature*, 521, 436  
 [11]. Goodfellow, I., Bengio, Y., Courville, A., & Bengio, Y. 2016, *Deep learning* (MIT press Cambridge)  
 [12]. Galvez, R., Fouhey, D. F., Jin, M., et al. 2019, *ApJS*, 242, 7  
 [13]. He, K., Zhang, X., Ren, S., & Sun, J. 2016, in *Proceedings of the IEEE conference on computer vision and pattern recognition*, 770–778  
 [14]. Ronneberger, O., Fischer, P., & Brox, T. 2015, in *International Conference on Medical image computing and computer-assisted intervention*, Springer, 234– 241  
 [15]. Karras, T., Aila, T., Laine, S., & Lehtinen, J. 2017, arXiv preprint arXiv:1710.10196  
 [16]. [Olga Andreeva](#), [Valentina Abramenko](#) and [V.M. Malaschuk](#), 11-year dynamics of coronal hole and sunspot areas <http://dx.doi.org/10.1515/astro-2022-0005>  
 [17]. Fox, Karen (19 July 2013). "[Large Coronal Hole Near the Sun's North Pole](#)". NASA. Archived from [the original](#) on 12 November 2020. Retrieved 31 October 2014.